Experimental investigation of NIRS spatial sensitivity

Amol V. Patil,[1,2,*] **Javad Safaie,**[1] **Hamid Abrishami Moghaddam,**[1,3]
Fabrice Wallois,[1,4] **and Reinhard Grebe**[1]

[1]*GRAMFC EA 4293, Fac. Medicine, University of Picardie Jules Verne, Amiens, France*
[2]*Indian Institute of Technology, Bombay, India*
[3]*Electrical Engineering Department, K. N. Toosi University of Technology, Teheran, Iran*
[4]*GRAMFC EA 4293, EFSN Pediatrique, North Hospital, Amiens, France*

*amolpatil.iitb@gmail.com

http://www.u-picardie.fr/labo/UGBM/

Abstract: Near infrared spectroscopy (NIRS) is regarded as a potential medical diagnostic technique for investigation of hemodynamic changes. However, uncertainties pertaining to the origin of NIRS signals have hampered its clinical interpretation. The uncertainities in NIRS measurements especially in case of living tissues are due to lack of rigorous combined theoretical-experimental studies resulting in clear understanding of the origin of NIRS signals. For their reliable interpretation it is important to understand the relationship between spatial changes in optical properties and corresponding changes in the NIRS signal. We investigated spatial sensitivity of near infrared optical measurements using an experimental approach. It uses a liquid optical phantom as tissue equivalent, which is explored under robot-control by a small, approximately point like perturbation of desired optical properties, and a NIRS instrument for trans-illumination/reflection measurements. The experimentally obtained sensitivity has been analyzed and compared with numerical simulations. In preliminary experiments we investigated the influence of various optical properties of the medium and of source/detector distances on the spatial sensitivity distribution. The acquired sensitivity maps can be used to define characteristic parameters. As an example, we used a 25% threshold to define a penetration depth measure which provides values in good accordance with published ones. To the best of our knowledge this is the first experimental study of NIRS spatial sensitivity. The presented method will allow in depth experimental investigation of the influence of various conditions pertaining to medium such as optical properties of tissue (scattering and absorption) and of the source/detector configuration.

© 2011 Optical Society of America

References and links

1. F. F. Jöbsis, J. H. Keizer, J. C. LaManna, and M. Rosenthal, "Reflectance spectrophotometry of cytochrome aa3 in vivo," J. Appl. Physiol. **43**, 858–872 (1977).

2. A. Villringer, J. Planck, C. Hock, L. Schleinkofer, and U. Dirnagl, "Near infrared spectroscopy (nirs): a new tool to study hemodynamic changes during activation of brain function in human adults," Neurosci. Lett. **154**, 101–104 (1993).

3. T. Kato, A. Kamei, S. Takashima, and T. Ozaki, "Human visual cortical function during photic stimulation monitoring by means of near-infrared spectroscopy," J. Cereb. Blood. Flow Metab. **13**, 516–520 (1993).

4. T. Näsi, K. Kotilahti, T. Noponen, I. Nissilä, L. Lipiäinen, and P. Meriläinen, "Correlation of visual-evoked hemodynamic responses and potentials in human brain," Exp. Brain Res. **202**(3), 561–570 (2010).

5. K. Sakatani, S. Chen, W. Lichty, H. Zuo, and Y. P. Wang, "Cerebral blood oxygenation changes induced by auditory stimulation in newborn infants measured by near infrared spectroscopy," Early Hum. Dev. **55**, 229–236 (1999).

6. H. Bortfeld, E. Wruck, and D. A. Boas, "Assessing infants' cortical response to speech using near-infrared spectroscopy," Neuroimage **34**, 407–415 (2007).

7. C. Hirth, H. Obrig, K. Villringer, A. Thiel, J. Bernarding, W. Mühlnickel, H. Flor, U. Dirnagl, and A. Villringer, "Non-invasive functional mapping of the human motor cortex using near-infrared spectroscopy," Neuroreport **7**, 1977–1981 (1996).

8. S. Boden, H. Obrig, C. Köhncke, H. Benav, S. P. Koch, and J. Steinbrink, "The oxygenation response to functional stimulation: is there a physiological meaning to the lag between parameters," Neuroimage **36**, 100–107 (2007).

9. M. Morihiro, T. Tsubone, and Y. Wada, "Relation between nirs signal and motor capability," Conf. Proc. IEEE Eng. Med. Biol. Soc. **2009**, 3991–3994 (2009).

10. A. J. Fallgatter and W. K. Strik, "Frontal brain activation during the wisconsin card sorting test assessed with two-channel near-infrared spectroscopy," Eur. Arch. Psychiatry Clin. Neurosci. **248**, 245–249 (1998).

11. K. Matsuo, N. Kato, and T. Kato, "Decreased cerebral haemodynamic response to cognitive and physiological tasks in mood disorders as shown by near-infrared spectroscopy," Psychol. Med. **32**, 1029–1037 (2002).

12. T. Suto, M. Fukuda, M. Ito, T. Uehara, and M. Mikuni, "Multichannel near-infrared spectroscopy in depression and schizophrenia: cognitive brain activation study," Biol. Psychiatry **55**, 501–511 (2004).

13. M. Kameyama, M. Fukuda, T. Uehara, and M. Mikuni, "Sex and age dependencies of cerebral blood volume changes during cognitive activation: a multichannel near-infrared spectroscopy study," Neuroimage **22**, 1715–1721 (2004).

14. S. D. Power, T. H. Falk, and T. Chau, "Classification of prefrontal activity due to mental arithmetic and music imagery using hidden markov models and frequency domain near-infrared spectroscopy," J. Neural Eng. **7**, 26002 (2010).

15. K. Sahlin, "Non-invasive measurements of O_2 availability in human skeletal muscle with near-infrared spectroscopy," Int. J. Sports Med. **13**(1), S157–S160 (1992).

16. F. Costes, J. C. Barthelemy, L. Feasson, T. Busso, A. Geyssant, and C. Denis, "Comparison of muscle near-infrared spectroscopy and femoral blood gases during steady-state exercise in humans," J. Appl. Physiol. **80**, 1345–1350 (1996).

17. L. M. K. Chin, G. J. F. Heigenhauser, D. H. Paterson, and J. M. Kowalchuk, "Pulmonary O_2 uptake and leg blood flow kinetics during moderate exercise are slowed by hyperventilation-induced hypocapnic alkalosis," J. Appl. Physiol. **108**(6), 1641–1650 (2010).

18. H. Habazettl, D. Athanasopoulos, W. M. Kuebler, H. E. Wagner, C. Roussos, P. D. Wagner, J. Ungruhe, S. G. Zakynthinos, and I. Vogiatzis, "Near-infrared spectroscopy and indocyanine green derived blood flow index for non-invasive measurement of muscle perfusion during exercise," J. Appl. Physiol. **108**(4), 962–967 (2010).

19. M. Xia, V. Kodibagkar, H. Liu, and R. P. Mason, "Tumour oxygen dynamics measured simultaneously by near-infrared spectroscopy and 19f magnetic resonance imaging in rats," Phys. Med. Biol. **51**, 45–60 (2006).

20. S. Nioka and B. Chance, "Nir spectroscopic detection of breast cancer," Technol. Cancer Res. Treat. **4**, 497–512 (2005).

21. M. Firbank, M. Oda, and D. T. Delpy, "An improved design for a stable and reproducible phantom material for use in near-infrared spectroscopy and imaging," Phys. Med. Biol. **40**, 955–961 (1995).

22. M. Firbank, E. Okada, and D. T. Delpy, "Investigation of the effect of discrete absorbers upon the measurement of blood volume with near-infrared spectroscopy," Phys. Med. Biol. **42**, 465–477 (1997).

23. H. Liu, B. Chance, A. H. Hielscher, S. L. Jacques, and F. K. Tittel, "Influence of blood vessels on the measurement of hemoglobin oxygenation as determined by time-resolved reflectance spectroscopy," Med. Phys. **22**, 1209–1217 (1995).

24. E. Okada and D. T. Delpy, "Near-infrared light propagation in an adult head model. ii. effect of superficial tissue thickness on the sensitivity of the near-infrared spectroscopy signal," Appl. Opt. **42**, 2915–2922 (2003).

25. E. Okada, M. Firbank, M. Schweiger, S. R. Arridge, M. Cope, and D. T. Delpy, "Theoretical and experimental investigation of near-infrared light propagation in a model of the adult head," Appl. Opt. **36**, 21–31 (1997).

26. S. R. Arridge, "Optical tomography in medical imaging," Inv. Probl. **15**, R41 (1999).

27. B. W. Pogue and M. S. Patterson, "Review of tissue simulating phantoms for optical spectroscopy, imaging and dosimetry," J. Biomed. Opt. **11**, 041102 (2006).

28. M. Tomita, M. Ohtomo, and N. Suzuki, "Contribution of the flow effect caused by shear-dependent rbc aggregation to nir spectroscopic signals," Neuroimage **33**, 1–10 (2006).

29. M. Tomita, "Flow effect impacts nirs, jeopardizing quantification of tissue hemoglobin," Neuroimage **33**, 13–16 (2006).
30. H. Dehghani, B. R. White, B. W. Zeff, A. Tizzard, and J. P. Culver, "Depth sensitivity and image reconstruction analysis of dense imaging arrays for mapping brain function with diffuse optical tomography," Appl. Opt. **48**, D137–D143 (2009).
31. T. Correia, A. Banga, N. L. Everdell, A. P. Gibson, and J. C. Hebden, "A quantitative assessment of the depth sensitivity of an optical topography system using a solid dynamic tissue-phantom," Phys. Med. Biol. **54**, 6277–6286 (2009).
32. A. Torricelli, A. Pifferi, P. Taroni, E. Giambattistelli, and R. Cubeddu, "In vivo optical characterization of human tissues from 610 to 1010 nm by time-resolved reflectance spectroscopy," Phys. Med. Biol. **46**, 2227–2237 (2001).
33. F. Faris, M. Thornley, Y. Wickramasinghe, R. Houston, P. Rolfe, N. Livera, and A. Spencer, "Non-invasive in vivo near-infrared optical measurement of the penetration depth in the neonatal head," Clin. Phys. Physiol. Meas. **12**, 353–358 (1991).
34. R. Liu, X. Liu, F. Scopesi, G. Serra, J. W. Sun, and P. Rolfe, "Spatial sensitivity of nirs tissue oxygenation measurement using a simplified instrument," in "7th Asian-Pacific Conference on Medical and Biological Engineering," vol. 19 of *IFMBE Proceedings* (2008), vol. 19 of *IFMBE Proceedings*, pp. 377–380.
35. G. Taga, F. Homae, and H. Watanabe, "Effects of source-detector distance of near infrared spectroscopy on the measurement of the cortical hemodynamic response in infants," Neuroimage **38**, 452–460 (2007).
36. T. J. Germon, P. D. Evans, N. J. Barnett, P. Wall, A. R. Manara, and R. J. Nelson, "Cerebral near infrared spectroscopy: emitter-detector separation must be increased," Br. J. Anaesth. **82**, 831–837 (1999).

1. Introduction

NIRS was first applied for in-vivo use in 1977 [1]. Since this discovery of the NIRS window (700–1300 nm) into the body, it has been widely used for measurement of tissue oxygenation. Part of those studies aimed to investigate various types of brain activation [2] due to stimuli as visual [3, 4], auditory [5, 6], motor [7–9] and more recently various cognitive [10–14] ones. Other fields of application include studies of blood perfusion in muscles [15–18] and in breast cancer [19, 20]. The main measure obtainable by NIRS is the tissue concentration of oxygenated and deoxygenated hemoglobin.

Even after two decades of intensive work of further development for acquisition and evaluation of NIRS, it is not yet really accepted as a diagnostic technique for clinical routine. This is mainly due to quantitative and spatial localization uncertainties so far typical for NIRS signals. To overcome these disadvantages important efforts have been taken to characterize various aspects of NIRS signals using different theoretical and experimental means. Experimental approaches using a tissue equivalent optical phantom [21–23] provided valuable insights in NIRS signal properties such as effects related to the redistribution of blood volume as resulting from changes in local vessel diameters affecting the optical properties of various tissue layers [24]. Theoretical models are of special interest because they can provide information about experimentally indeterminable parameters like partial optical path length [25]. For tissue like medium there exists an excellent theoretical framework concerning the spatial sensitivity of NIR optical measurements [26]. However, these spatial sensitivity maps have until now neither been experimentally investigated nor explicitly verified. A review of tissue simulating phantoms for optical spectroscopy, imaging and dosimetry is given by [27].

This work establishes the first report concerning the direct investigation of NIRS spatial sensitivity profiles for simple geometric cases. We present an experimental method and a protocol for investigating spatial sensitivity of NIRS under various conditions. The paper elaborates methodology and design of according experiments. This concerns mainly selection of phantom material, geometry and experimental protocol.

2. Spatial sensitivity of NIRS

Biological tissue acts as absorbing and scattering medium for near infrared light. For this type of medium the diffusion approximation of radiative transport equation (RTE) has been used

successfully. The frequency domain form of the diffusion equation is given as

$$-\nabla D(r) \cdot \nabla \Phi(r, \omega) + \left(\mu_a(r) + \frac{j\omega}{c} \right) \Phi(r, \omega) = f(r, \omega), \tag{1}$$

where Φ is the radiative fluence, D the diffusion coefficient given by $D = 1/(3 \cdot (\mu_a + \mu_s'))$, μ_a and μ_s' are absorption and reduced scattering coefficient, respectively, ω is the modulation frequency of the source and r is the spatial position.

Boundary conditions are given by

$$\Phi(r, \omega) - 2A \cdot n \cdot D(r) \cdot \nabla \Phi(r, \omega) = 0, \tag{2}$$

where A is a factor accounting for refractive index mismatch on the boundary.

Another popular and more generic model for such light transport is based on Monte-Carlo simulations. In the Monte-Carlo method the interaction of light with matter is treated as a stochastic process where each randomly selected interaction causes a random change in direction of the path of photon propagation as well as of the power.

The spatial sensitivity has been described theoretically by photon measurement density functions (PMDF) or sensitivity maps. Arridge et al. have described a computationally efficient method for computing PMDF using a perturbation approach and an adjoint source model [26]. We have carried out our simulation using this theoretical model.

In biomedical applications this is used for computation of chromophore concentrations based on the modified Beer-Lambert's law. Oxygenated hemoglobin (HbO) and reduced hemoglobin (HbR) are the two main chromophores of interest for NIRS. The modified Beer-Lambert's relation is given by

$$I_d^\lambda = I_s^\lambda \exp\left(-\left(\mu_a^\lambda + \mu_s'^\lambda \right) \cdot PL \right), \tag{3}$$

where I_s^λ and I_d^λ are the source and the detected intensity at the detector site for wavelength λ, μ_a^λ and $\mu_s'^\lambda$ are effective absorption and reduced scattering coefficients as experienced by the photon transport, PL is the mean path length of the photon trajectories from source to detector and, G is a geometric loss factor accounting for photons lost due to scattering and geometrical constraints.

μ_a^λ is related to Hb, HbO concentrations as a weighted sum with the weighting factors extinction coefficients $\varepsilon_{HbO}^\lambda$ and, $\varepsilon_{HbR}^\lambda$

$$\mu_a^\lambda = \varepsilon_{HbO}^\lambda [HbO] + \varepsilon_{HbR}^\lambda [HbR.] \tag{4}$$

In case of scattering medium like tissue, PL is larger than the distance between source and detector. This enlargement of the photon path is due to multiple scattering of photons which is parametrized by $\mu_s'^\lambda$. It is generally assumed that $\mu_s'^\lambda$ is invariant for physiological changes like regional cerebral blood flow (rCBF) changes and relevant blood volume (rBV) changes. However, there are studies reporting scattering changes as significant as absorption related to rCBF and rBV changes, which are basically due to the pronounced differences in scattering between a solution of single red blood cells, red blood cell aggregates and a hemoglobin solution [28, 29].

If we assume that scattering changes are invariant during measurements, we can model the mean photon path length PL as $PL = l \cdot DPF$ where DPF is the differential path length factor. $DPF = PL/l$ is assumed to be constant for particular optical properties and hence tissue types.

With these set of assumptions, Eq. (3) takes the form most widely used in NIRS

$$I_d^\lambda = I_s^\lambda \exp\left(-\mu_a^\lambda \cdot l \cdot DPF \right), \tag{5}$$
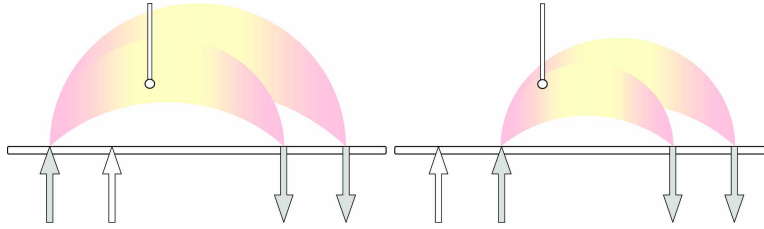
Fig. 1. Principle idea of the experimental setup to determine NIRS sensitivity.

Fig. 2. Principal components of the experimental setup:
- front: the tank containing the liquid phantom,
- right: the scanning unit with attached probe,
- left: the NIRS-acquisition system,
- back: the control and data acquisition unit (laptop).

where the absorption μ_a^λ is computed by

$$\mu_a^{*\lambda} = \frac{1}{l \cdot DPF} \cdot \ln\left(\frac{I_s^\lambda}{I_d^\lambda}\right) = \frac{1}{l \cdot DPF} OD^\lambda. \tag{6}$$

3. Material and method

The basic idea of our experimental approach is presented in Fig. 1.

The scheme of the experimental set-up is shown in Fig. 3. It consists mainly of four components: optical tissue phantom, 3D scanning unit, NIRS instrument and control and data acquisition unit (PC).

3.1. Experimental setup

The dynamic optical tissue phantom consists of two major components, a background optical phantom and an optical perturbation. The background optical phantom is realized as a liquid filled tank ($20x20x20cm^3$), Fig. 3(a). The use of a liquid tissue phantom allows for
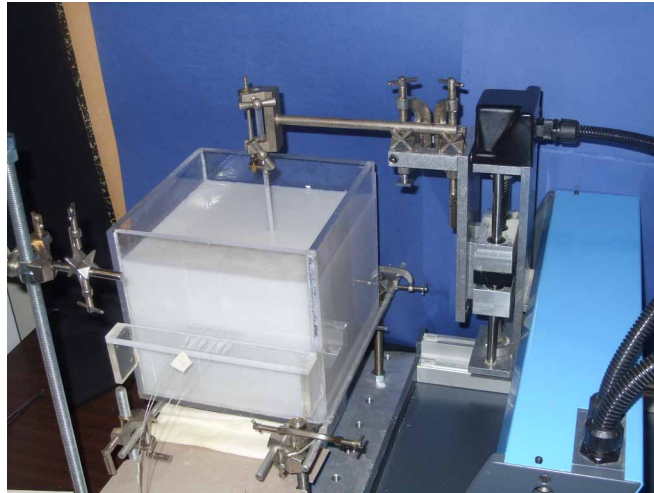
(a) Scanning unit with attached probe immersed in phantom = tank with liquid.
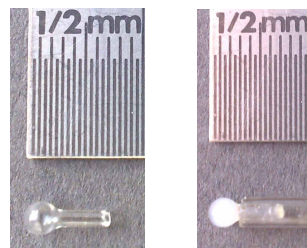
(b) Perturbation, left: empty bulb, right: filled and fixed to holder.

Fig. 3. The experimental setup.

free positioning and moving of the optical perturbation inside the phantom volume. In addition, a liquid phantom is suitable for changing optical properties. Ingredients of the liquid phantom are distilled water, 'Medialipid 20%' (B.Braun Medical) and 'India Ink' (Lefranc & Bourgeois). The concentration of Intralipid and india ink is chosen to achieve various optical parameter values as needed for the experiments. For our purposes we have chosen concentrations resulting in mean optical properties as typical for tissues as reported in literature i.e. $\mu_a^\lambda = 0.001 \pm 0.0002 mm^{-1}$ for 'normal' effective absorption and $\mu_s'^\lambda = 0.8 \pm 0.05 mm^{-1}$ for normal reduced scattering [30–32]. To avoid any sedimentation effects a magnetic stirrer is turning continuously throughout the whole experiment.

The optical perturbation is realized by a liquid-filled glass bulb, see Fig. 3(b). This home made glass bulb is thin walled ($\sim 0.2mm$ thick) and spherical shaped (1 mm diameter) with a tubular opening (0.2mm internal diameter). The liquid in the glass bulb can be freely chosen to meet the desired optical properties normally with respect to the liquid of the background. The glass bulb end is closed using silica gel (glass adhesive). It is held in position using a L-shaped glass tube, which is filled with the same liquid as used for the background tissue phantom.

The NIRS system used is a frequency domain instrument (Imagent^{TM} from ISS inc) with a modulation frequency of 110 MHz. However, only DC intensity measurements are used in this work. Optical glass fibers are used as emitters and detectors. Refraction effects due to transparent perspex walls are avoided by holes drilled into the wall of the tissue phantom tank
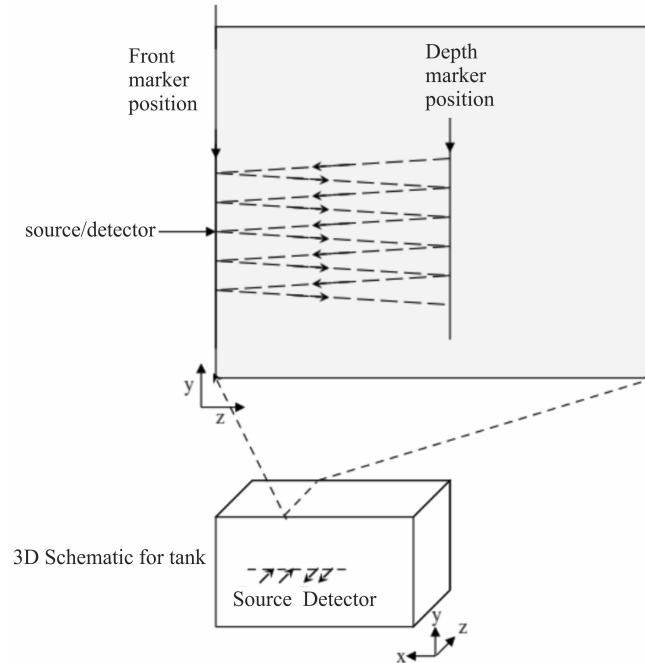
Fig. 4. Scanning trajectory for a plane in Y-Z plane.

to position the tips of the optical fibers at the internal tank surface. This arrangement is also helpful in mimicking the fiber contact with skin. For the current experiments two sources and two detectors are used in the configuration as shown in Fig. 2.

For interactive and fully automatic 3D positioning and scanning a multipurpose precision machine is used (Profiler Pro, Colinbus inc.) with $0.1mm$ position resolution. The perspex glass tank is fixed on a rigid support at a well calibrated position with respect to the 3D position manipulator. The support tube of the perturbation is mechanically fixed to the 3D positioning head of the manipulator.

3.2. Measurement protocol

The experimental protocol is designed to determine the light intensity distribution inside a pre-defined volume of the medium with a reasonable resolution. Therefore, the multipurpose machine is programmed to scan the desired volume with the optical perturbation while performing continuous optical intensity measurements via the emitter/detector pairs.

The moving perturbation followed a raster scan pattern in a two dimensional vertical plane perpendicular to the tank wall in which source and detector were fixed, see Fig. 4. After scanning one plane, the adjacent plane (1mm apart) was scanned using the same raster scanning pattern. This scanning protocol was repeated to cover a rectangular block volume.

With this scanning protocol a sufficient spatial resolution with a good reproducibility was achieved for the three dimensional region of interest. At the end of each scan line, a synchronization impulse was generated and recorded along with the optical intensity signal. These synchronization signals are referred as *front markers* and *depth markers* as shown in Fig. 4. These signals are important for synchronizing the NIRS measurements with the movement of the perturbation, it allows precise determination of the position of every measurement taken inside the
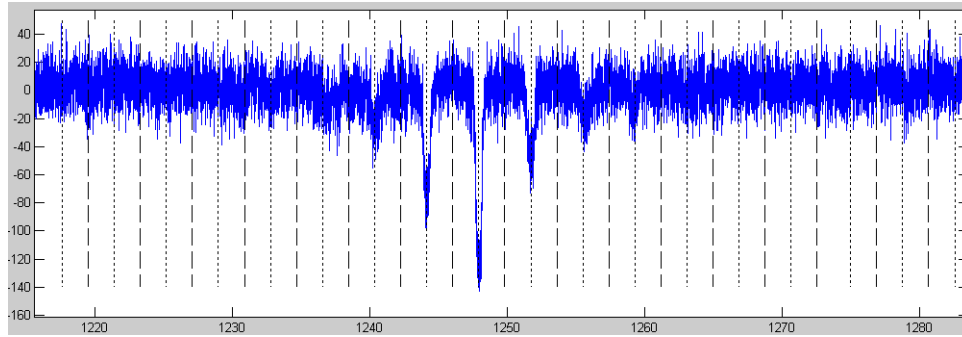
Fig. 5. Part view of raw scan data after detrending ('. . . .' Front marker, '- - -' Depth marker).

scanned volume (Fig. 5). The speed of movement of the perturbation was fixed ($10mm/sec$) and kept in principle over the whole time of recording. However,stopping of probe movement and change in direction causes variation in speed. These changes have been determined and corresponding correction are applied during data processing.

For every measurement scan, a control scan was performed in addition to determine effects of the supporting glass components necessary to hold the inclusion in place. For this purpose the perturbation - the glass bulb - and the "L" shape holding glass pipe were filled with the same liquid as used for the background tissue phantom.

3.3.   *Data acquisition and signal processing*

Data acquisition and storage   Data is acquired performing two scans as described before. After the reference scan, the glass bulb is filled with background liquid containing the added optical perturbation. This perturbation can be chosen as desired either as absorption perturbation or as scattering or both. Results from these scans are two series of sequential data containing the complete information of a spatial sensitivity distribution.They are stored for further evaluation together with the according synchronization data acquired from the scanning unit. For each source detector pair a sampling frequency of 138.8 samples per second is used for acquisition.

Removal of baseline drift   Before decomposition of the data stream in lines the first preprocessing steps are low pass filtering and detrending. A slow drift was observed in all measurements, the nature of which was studied using multiple trial recordings. It turned out to be extremely slow but not reproducible. The most likely and probably most important source of such drift may be the photomultiplier of the NIRS instrument. To detrend the acquired signals we proceeded as follows.

The acquired signal consists of a sequence of scanning lines starting from the foreground 'Front marker position' containing mainly the interesting signal and ending at the 'Depth marker position' containing in principle constant background noise only. Since this background noise should be constant over the whole volume (care has been taken to have e.g. no jeopardizing light sources in the system) part of the signal around the depth marker is taken for detrending. For this purpose we use a 0.5 second window around any depth marker to determine the local level of mean background noise. The series of these means provides the trend curve which is then subtracted from the raw signal.

Conversion of raw scan data into a 3D-image   Using the synchronization data 'Front marker' and 'Depth marker' the raw data stream is splitted into lines. For each of this a correction is necessary to compensate the change in propagation speed of the probe at the end of each line scan. Then these lines are put together to form the slices and from the slices the according 3D data volume is created after additional adequate interpolation to achieve a data space of isotropic resolution.
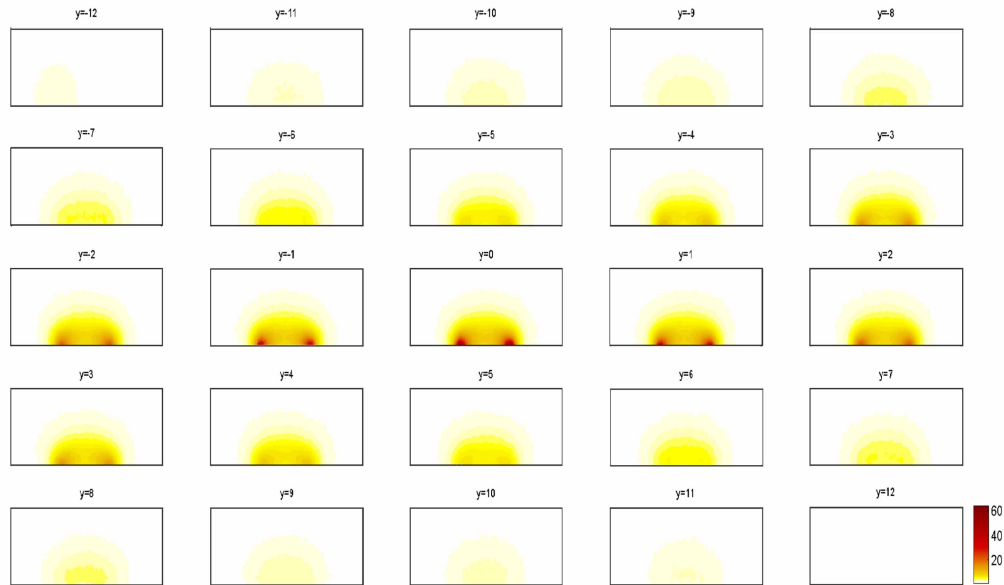

Fig. 6. Volume scan presented as sequence of x-z slices for a control scan with y=0 at the source-detector connection line.

Creation of the sensitivity map   The steps for the creation of the actual sensitivity map as visualized in Fig. 7 are:

1. Control scan acquisition and creation of the background reference 3D map,

2. Perturbation scan acquisition and creation of the raw sensitivity map,

3. Sensitivity map calculation as the difference between the raw sensitivity map and the background reference map.
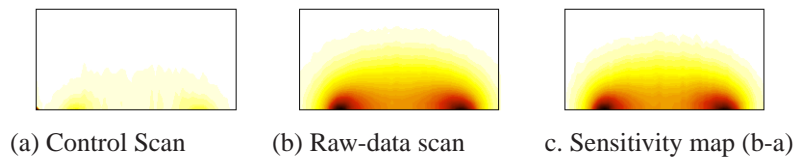

(a) Control Scan   (b) Raw-data scan   c. Sensitivity map (b-a)

Fig. 7. Sensitivity map creation: elimination of glass holder effect exemplary demonstrated with slice y=0.
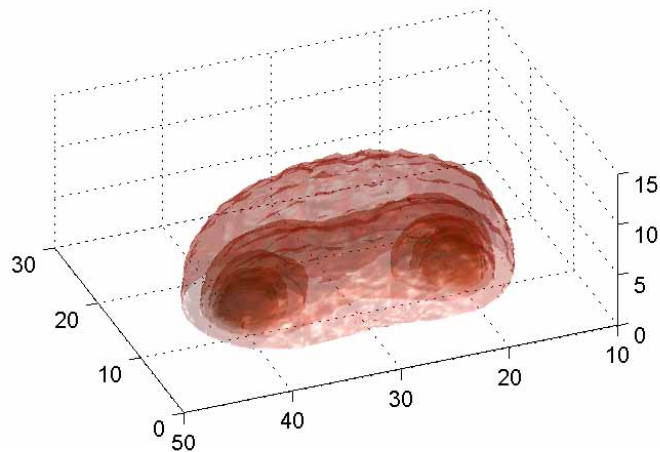
Fig. 8. Surfaces of photon iso-activity for a source detector distance of 20 mm.

3.4. *Model and simulations*

The PDE for the diffusion approximation of the radiative transport equation (RTE), chapter 2 Eq. (1), is numerically solved using the finite element method (FEM). For model creation and simulation we use the Matlab based FEM package FEMLAB (Comsole inc.). For every simulation the dimensions of the actual experimental setup including geometry of the optical phantom and positions of sources and detectors were used to create a model mimicking the real situation as closely as possible.

Model   A rectangular prism of dimension $20x20x18cm^3$ is used as a model for the tank filled with liquid phantom. Source detector positions are the same as used for the experiments. The complete geometry is described by a tetrahedral mesh. The mesh resolution is adapted to the local needs, higher than background for the area of scanning and highest near the sources and detectors (maximum edge length $0.5mm$). The model has been implemented as described.

Simulations   Simulations have been carried out on a PC with 2 quad core CPUs and 16 GB of RAM.

4.   Results

Experiments have been carried out following the above protocol using different background optical properties and different type of perturbations resulting in sensitivity maps. According boundaries and properties have been fed into the above described modeling and simulation procedure providing diffusion approximation based simulation results which are compared with the corresponding experimental results. Considering the region of validity of diffusion approximation only the part above the approximate mean free scattering path is presented for comparison. To visualize in 3D the characteristics of the spatial sensitivity distribution as detected by our system Fig. 8 presents a sequence of five subsequent iso-sensitivity surfaces (transparent).
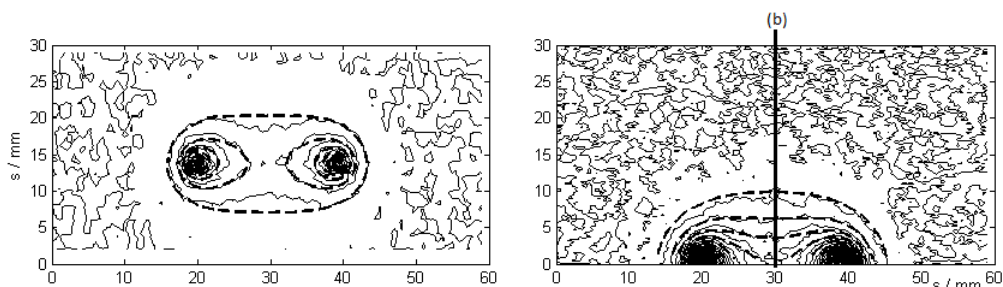
(a) left: top view (x/y plane) of light injection (20/15) and detection (40/15); right: side-view (x/z plane) of light injection (20/0) and detection (40/0); relative sensitivity difference between neighboring contour lines is 2.5%.
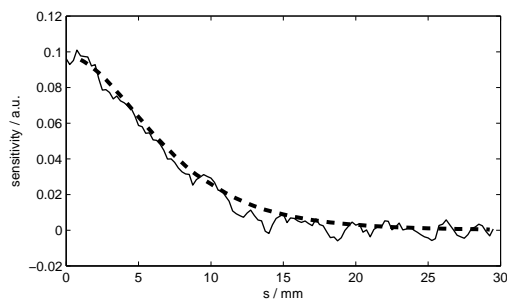
(b) Sensitivity decline in direction of the perpendicular bisector of the emitter-detector connection (bar in above figure (right) originating from (30/0)).

Fig. 9. Comparison of results from experiments (solid thin lines) and simulations (thick dashed lines). Experiments have been carried out in a background medium of 'normal' scattering and absorption. According parameter values have been entered in the simulation (emitter-detector distance: 20mm).

4.1. Comparison: experiment and simulation

In first experiments we compared theoretically predicted and experimentally determined sensitivity distributions for different absorption coefficients of the medium. Figure 9 presents the combined results from a typical experiment and simulation here for a background medium with normal scattering and absorption as defined before. Figure 9(a) gives the top and side view of the interesting part of the sensitivity map around the emitter and detector where the scalar fields are presented by isopotential lines of sensitivity values, thick regular lines stemming from simulation and thin ones from experiment. A good qualitative accordance between the field characteristics of the two can be stated.

For further, more quantitative comparison, the sensitivity decline in direction of the perpendicular bisector of the emitter - detector connection has been determined for the same set of experiment and simulation. This presentation provides quantitative information about the penetration depth (see Chap. 4.4) which is of special interest for numerous applications. The good accordance between experiment and simulation is confirmed.

4.2. Background absorption

To get an idea about the influence of background absorption on the propagation of light in a reasonably scattering medium, experiments have been carried out to compare sensitivity maps
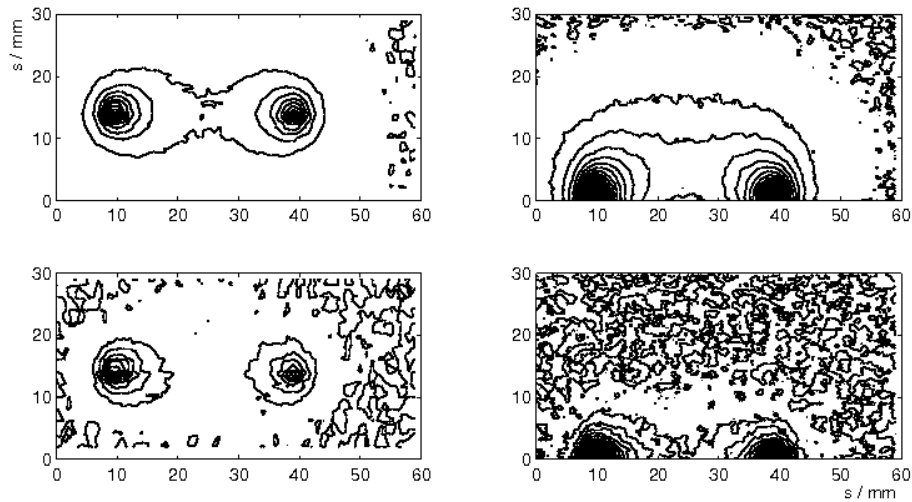
Fig. 10. Comparison of results from experiments with different background medium: upper row 'normal' scattering and low (half normal) absorption, lower row 'normal' scattering and high (doubled) absorption. The left hand side gives the lower topview, the right the middle cross section. The distance between emitter and detector has been 20mm.

between media of 'normal' scattering containing in the first experiment a low (half of the normal) concentration of absorbing molecules, which has been doubled for the second. The results in Fig. 10 show, as to be expected, that in the medium of lower absorption (Fig. 10 upper row) much more of the detected photons have passed much longer tracks much deeper in the volume than in the one of doubled absorption (Fig. 10 lower row).

4.3. Source-detector distance

Another set of experiments has been dedicated to the influence of the distance between source and detector on light propagation in a certain medium and thus on the sensitivity map (Fig. 11).

The sensitivity mappings in Figs. 11(a)–11(c) present results from experiments, which have been performed with source-detector distances of 20 mm, 30 mm and 40mm presented from top to down each with a top- (left) and a side-view (right). Comparing the side views for the different distances one mentions the higher density of iso-sensitivity lines near and between the source and detector for the short distance indicating a quicker decline than for the greater distances. This becomes even more obvious when comparing sensitivity on the perpendicular bisectors of the source-detector connection (Fig. 12 upper part).

4.4. Penetration depth

Penetration depth may be characterized by evaluating the courses passed by the photons on their way from source to detector. So, evaluating the distribution of passages of all photons through a certain barrier should provide according information. As such barrier we use the bisector of the line connecting source and detector perpendicular to the ground plane. The more photons pass this barrier the farer from its origin the higher should be the penetration depth. Since the sensitivity distribution is determined from the number of photons passing through differential volumes one can use for an according evaluation directly the sensitivity map.

Thus, for a more quantitative treatment of the phenomenon observed in the experiments
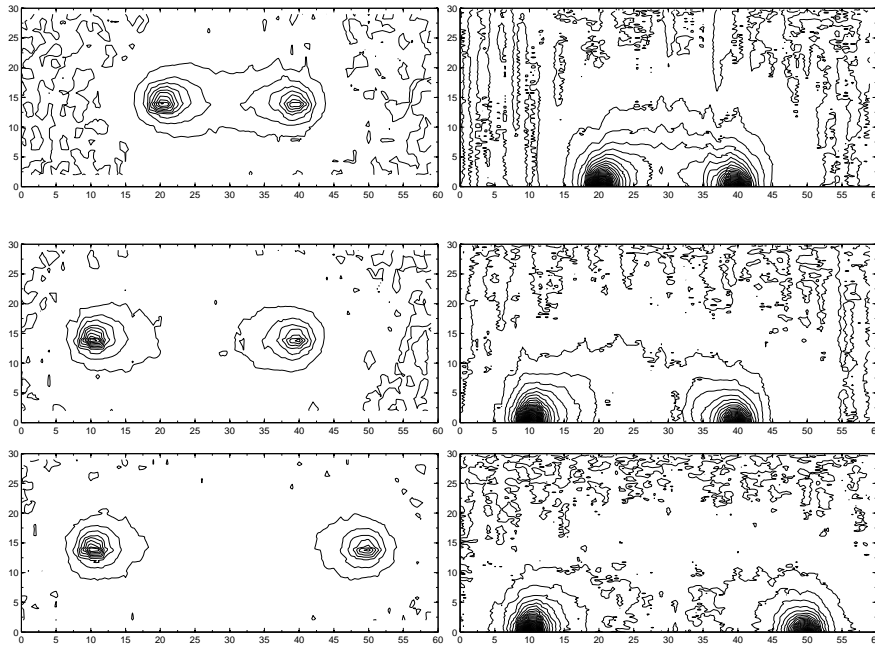
Fig. 11. Sensitivity maps for different source-detector distances with the same scattering and absorption of the background.

and described in the preceding sub-chapter an evaluation in terms of this penetration depth of the signal into the tissue has been performed. As in chapter 4.1 in a first step the sensitivity decline in direction of the perpendicular bisector of the emitter-detector connection has been determined as function of the distance from the bottom plate (upper part of Fig. 12). Then the sensitivity data for each curve has been normalized to the individual total area under the curve (middle part of Fig. 12). From these the curves of accumulated activities have been determined (lower part of Fig. 12). The 75% line of cumulated activity allows to determine a penetration depth measure for the different source-detector distances: D20:∼10mm, D30:∼13mm, D40:∼15mm. For every source-detector distance 25% of the information contained in the signal is stemming from parts farer from the probes than the determined distance.

5. Discussion

In general a 3D-map of optical sensitivity should provide a scalar field distribution of sensitivity for an entire space including absorption and scattering with a sufficiently high resolution. Such three dimensional sensitivity distribution would allow to determine directly the effect of changes of local optical properties anywhere in the space on the signal acquired by the measurement system. It is important to mention that the sensitivity distribution is not an object property only but depends also highly on the measurement configuration as position of the optodes and distances between them.

Obviously, existing phantoms and experimental approaches as presented before are far from allowing direct physical measurement of sensitivity distributions [30, 33–35]. Here our fluid phantom has the main advantage to allow scanning of the whole space of interest with relatively high resolution for both absorption and scattering independently or combined. From the acquired data complete high resolution sensitivity maps can be created.

Since we use a fluid phantom we can easily adapt its optical properties to what ever combi-
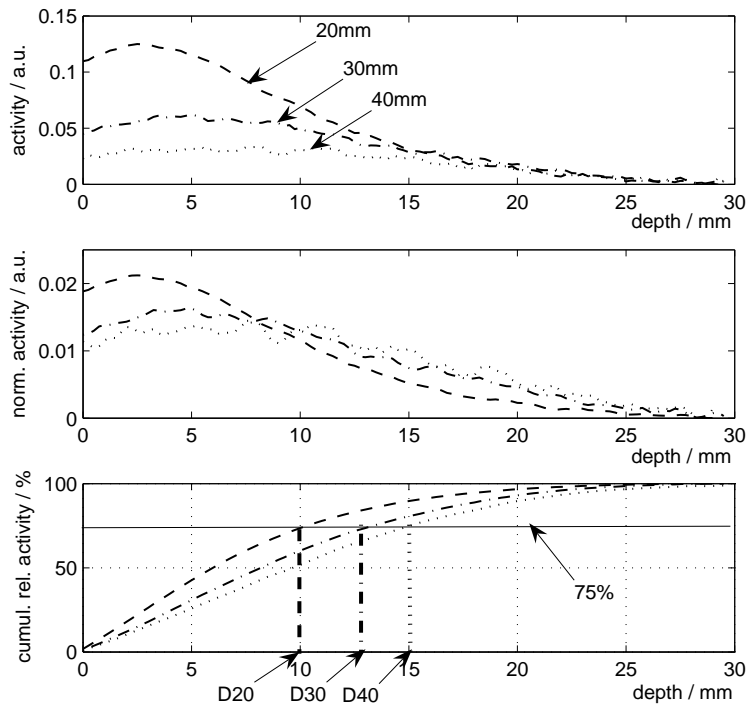
Fig. 12. Penetration depth measure for emitter-detector distances of 20, 30 and 40mm. Shown are the cross sections of the sensitivity map in the bisector plane of emitter-detector connection for experiments with low absorbing medium. From top to bottom are given: local sensitivity, sensitivity normalized to the individual total sensitivity, accumulated relative sensitivity. The 75% line of cumulated activity defines the penetration depth measure.

nation of absorption and scattering is needed. This is true for the scanning probe (perturbation) as well. The size of this probe is the limiting factor regarding the achievable resolution. The so far smallest glass bulb designed by us for this purpose has a diameter of 1mm (Fig. 3(b)). Since the step width of our scanning system is 0.1mm the effective resolution of our system should be sufficient to serve as model for almost all structures which may be of interest.

A principal problem of the developed setup is the need of a freely movable fixation for the probe inside the phantom. This fixation should be as solid as necessary to allow for precise positioning and as nonperturbing as possible. We use a glass tube for this purpose filled with the same medium as the actual phantom. This reduces the unavoidable perturbations but cannot avoid the perturbation by the glass. Since the scanning results show a very good reproducibility the influence of the undesired perturbations on the scan results can be eliminated by subtraction of a reference scan from the actual scan, see Fig. 7. This reference scan results in a sensitivity map which presents the sensitivity of the system to the moving glass parts of the probe fixation only. By comparing Fig. 7(a)–7(c) it becomes evident that the system is sensitive to these glass parts, that these sensitivity has to be eliminated and that this is successfully done with our approach.

Validation   The validation of a system like the here presented one is a difficult task because of the lack of an according gold standard. As a first global test Figs. 6 and 8 present 3D visualizations which correspond nicely to what would be expected for such a sensitivity map. This namely concerns the symmetry between emitter and detector and the development of equal sensitivity surfaces in the space.

For a more sophisticated validation we compared our measurements with results from simulations based on numerical models. Figure 9 gives a typical example of such an experiment where in the upper part in top- and side-view the smooth equi-sensitivity lines of the simulation correspond very good with the noise disturbed ones from the experiment. To mention is the noise which becomes visible in the experimental results in some distance of the optodes where the changes in sensitivity approach the signal to noise ratio of 1 and even less (Fig. 9(b)). A good congruence between the results from experiment and simulation can be stated and thus a certain validation for both methods.

First results   Two further experimental sets have been performed to demonstrate the usefulness of the presented phantom and the further possibilities to study in depth details of sensitivity distributions in different media and their meaning for application of NIRS. In the first set a simple demonstration of the effect of a twofold increase of absorbency in the medium was performed. As stated already, one of the interesting features of the sensitivity map is the appearance of noise in some distance from the optode pair indicating where the spatial sensitivity gradient becomes smaller than the noise amplitude. This borderline indicates consequently from whereon changes in optical properties as between actual background and probe are not anymore directly detectable. From Fig. 10 one could conclude as a first estimate that by doubling the absorption in the medium the depth from where information can be gathered decreases two to three times.

A more detailed analysis has been performed for the importance of the optode distance for the composition of the acquired signals. This is a topic of highest interest in all NIRS applications and a lot of theoretical work including modeling and simulations has been performed to treat this subject. Anyway, much less experimental work providing quantitative information is to be found in literature most often based on clinical experiments, which results are interpreted in qualitative manner to determine the effect of different source-detector spacing on the detected signals [34–36].

Obviously such work is and must stay qualitative. So, it would be highly desirable to be able to perform more in depth investigation illuminating the underlying principles allowing quantitative investigation concerning the light propagation etc.. The here presented sensitivity mapper is a tool which can provide detailed information about the sensitivity distribution for a wide range of configurations. As exemplary done in chapter 4.4 physical magnitudes may be defined and quantitatively evaluated. We invent here for this purpose the parameter penetration depth measure which now allows to compare quantitatively changes in signal composition due to different source-detector distances.

Table 1. Penetration Depth Measure as Function of Source-Detector Distance

	distance/mm	depth/mm
	20	10
	30	13
	40	15

Table 1 summarizes the results and Fig. 13 visualizes the penetration depth measure as a function of the chosen source-detector distance.
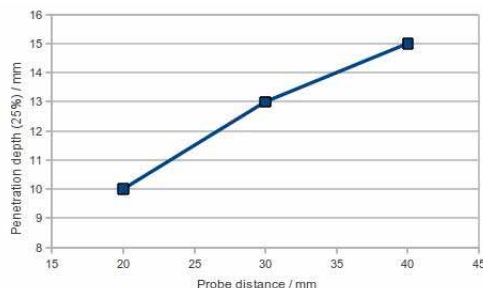
Fig. 13. Penetration depth measure as function of source-detector distance.

In conclusion one can state that with increasing distance between source and detector on the one hand, as to be expected, the amount of collected light decreases, on the other hand the relative amount of light and thus information from regions deeper in the volume increases. This means that the penetration depth increases with increasing source-detector distance. The values determined for the penetration depth measure are in good accordance with the one estimated for according measures in literature [30].

6. Conclusion

The presented phantom has proven to be an adequate tool to acquire three dimensional sensitivity maps for a wide variety of optical properties of media and perturbations and of source/detector configurations. The optical properties are namely absorption and scattering in any desired combination. This will allow to study under well defined experimental conditions the influence of e.g. oxygenation-deoxygenation of hemoglobin in terms of absorption as well as to discriminate the possible effect of changes in scattering on acquired signals as may be evocated by local changes in erythrocyte concentrations.

The possibility to create experimentally acquired spatial sensitivity maps may be the most important progress achieved with this type of phantom. Thus it is possible to verify and validate simulation results in detail by comparing the theoretical achieved sensitivity maps with the experimental ones as has been shown exemplary for different medium.

As has been further demonstrated physical parameters can be precisely defined allowing to characterize and compare quantitatively optical properties for different in vivo tissue configurations. Based on such information it will be possible to optimize measurement configurations as consisting of different source-detector pairs or verify according theoretical optimization results.

For further work it will be possible to create different phantom geometries, to incorporate subspaces in the phantom containing media of different optical properties, to create different types of perturbations and to perform even experiments dealing with dynamic changes of certain phantom properties.